Nanoscale

ROYAL SOCIETY OF CHEMISTRY

PAPER

View Article Online
View Journal | View Issue

Cite this: *Nanoscale*, 2025, **17**, 12162

Homogenization enabled efficient regeneration of spent Ni-rich $LiNi_xCo_yMn_{1-x-y}O_2$ cathodes†

Xiangjun Liu,‡[a,b] Penglei Yan,‡[c] Binglei Jiao,*[c] Guiling Wang,[a] Chunling Zhu,[a] Qiao Zhang,[c] Jinxing Chen[c] and Panpan Xu*[b]

Received 31st December 2024,
Accepted 10th March 2025

DOI: 10.1039/d4nr05509h

rsc.li/nanoscale

High-Ni $LiNi_xCo_yMn_{1-x-y}O_2$ (NCM) oxides with low Co content have emerged as promising candidates for next-generation cathodes due to their high energy density and acceptable manufacturing costs, making them widely adopted in electric mobility applications. However, their limited service life highlights an urgent need for efficient and economical recycling methods. Direct regeneration *via* relithiation has proven effective for the chemical restoration of degraded cathodes at low cost, but repairing high-Ni NCM cathodes remains challenging due to their degradation mechanisms of intergranular cracking and particle fragmentation. To overcome these challenges, we exploited the weakened interactions along grain boundaries in post-cycled NCM cathodes, achieving morphological reconstruction and size homogenization of degraded Ni-rich NCM through mild ball milling. The resulting NCM nanoparticles expose more facets for Li^+ diffusion compared with polycrystalline particles, effectively shortening the diffusion pathways during the subsequent relithiation process and enabling efficient regeneration at low temperatures and within short processing durations. This work provides valuable insights into designing effective repairing strategies for mechanically degraded cathodes, advancing the applicability of direct regeneration techniques and fostering the sustainable development of Li-ion batteries.

[a]*Key Laboratory of Superlight Materials and Surface Technology of Ministry of Education, Department of Materials Science and Engineering, Harbin Engineering University, Harbin, Heilongjiang, 150001, China*
[b]*Suzhou Institute of Nano-Tech and Nano-Bionics, Chinese Academy of Sciences, Suzhou, 215123, China. E-mail: panpanxu2021@sinano.ac.cn*
[c]*Institute of Functional Nano & Soft Materials (FUNSOM), Jiangsu Key Laboratory for Carbon-Based Functional Materials & Devices, Soochow University, Suzhou, 215123 Jiangsu, P. R. China. E-mail: bljiao@suda.edu.cn*

†Electronic supplementary information (ESI) available. See DOI: **https://doi.org/10.1039/d4nr05509h**

‡These authors contributed equally to this work.

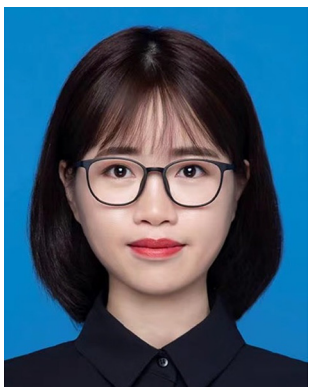

Panpan Xu

Panpan Xu, an Associate Professor at the Suzhou Institute of Nano-Tech and Nano-Bionics, CAS, earned her B.S. (2013) and Ph.D. (2018) in Materials Science from Harbin Engineering University and conducted research at UC San Diego (2018–2021) under Prof. Zheng Chen. Her research focuses on battery material failure mechanisms, defect repair, and the recycling of spent lithium-ion batteries, with over 40 SCI papers published as the first or corresponding author in Joule, Nature Communications, Advanced Functional Materials, and other high-impact journals.

Introduction

Under the pursuit of the "dual carbon goal", the transportation sector is rapidly transitioning toward electrification, with forecasts predicting 300 million electric vehicles (EVs) on the road by 2030.[1,2] However, the driving range of current EVs, powered by lithium-ion batteries (LIBs), remains insufficient to match that of internal combustion engine vehicles (ICEVs). This "range anxiety" has driven the development of LIB cathodes towards higher energy density. Ni-rich layered oxides with low Co content have emerged as next-generation cathodes due to their potential to achieve an energy density of ~800 W h kg^{-1}, while maintaining relatively low manufacturing costs. However, the high performance of these materials comes at the expense of long-term cycling stability, resulting in earlier retirement than the typical lifespan (5–8 years).[3,4] Consequently, it is urgent to develop efficient, environmentally friendly and cost-effective methods to recycle these batteries.

Currently, hydrometallurgical recycling, which relies on strong acids to dissolve cathodes and extract elemental products, is the most established method for recovering valuable materials from spent LIBs. While effective, it demands significant quantities of corrosive agents, generates large volumes of wastewater and becomes economically unfeasible for cathodes with minimal valuable elements like Co, due to high recycling costs.[4–6] In contrast, direct regeneration, which repairs

structural and compositional defects in spent cathodes without comprising their embedded energy, offers a more sustainable alternative. This approach directly produces cathode materials for battery assembly, rather than producing cathode precursors that require additional reprocessing.[7–9] Compared to conventional methods, direct regeneration streamlines the process, reducing costs and environmental impact.

While direct regeneration has proven effective for regenerating cathode materials such as $LiFePO_4$, $LiMn_2O_4$ and $LiNi_xCo_yMn_{1-x-y}O_2$ with Ni content below 60%, its application to high-Ni NCM materials remains challenging.[10,11] The degradation of Ni-rich cathodes involves atomic-scale issues, such as Li deficiencies and phase transformations, as well as microscale problems, such as intergranular cracking and particle fragmentation. These challenges cannot be fully addressed through conventional chemical relithiation or sintering alone.[12] Although a eutectic molten salt method has been proposed to recycle spent Ni-rich cathodes into single crystal particles *via* complete melting and recrystallization,[13,14] it requires large quantities of Li salts to form a homogeneous liquid phase, significantly increasing the cost of regeneration.

In this study, we present a two-step regeneration strategy involving ball milling pretreatment followed by short sintering to regenerate mechanically degraded $LiNi_{0.7}Co_{0.15}Mn_{0.15}O_2$ (NCM70) cathodes retired from electric bicycles. The ball milling process takes advantage of the naturally loosened grain boundaries in NCM after long-term cycling, with mild mechanical force effectively breaking secondary particles into uniform primary particles. The resulting NCM nanoparticles expose more facets for Li^+ diffusion, significantly shortening diffusion pathways and enabling efficient Li^+ replenishment at low temperatures and in short durations. By systematically optimizing the key regeneration parameters, including sintering temperature, duration, and Li source dosage, the capacity of the regenerated NCM cathode was significantly improved from 104.2 to 173.1 mA h g^{-1}. This work introduces a simple yet effective approach for regenerating degraded cathodes with irregular cracking, expanding the applicability of direct regeneration methods and contributing to the sustainable development of LIBs.

Experimental section

Collection of spent cathode materials

The waste battery was first discharged to 2 V and disassembled in a glove box filled with argon. After separation, the obtained cathode strips were rinsed with dimethyl carbonate (DMC) to remove any residual electrolyte and subsequently cut into small pieces, immersed in *N*-methyl-2-pyrrolidone (NMP) solvent and heated with stirring for 8 hours to completely dissolve the polyvinylidene fluoride (PVDF) binder. Afterward, solid/liquid separation was performed, and the collected black material was dried in a vacuum oven at 120 °C for 12 hours, resulting in the degraded NCM70 (DNCM70) material.

Homogenization and regeneration of the spent cathode

The DNCM70 powder was ground in ethanol at speeds of 450 rpm, 540 rpm, 630 rpm, and 750 rpm for 6 hours to achieve homogenized NCM materials (HDNCM70). These homogenized materials were then regenerated using a simple solid-state sintering method. Specifically, the HDNCM70 powder was uniformly mixed with a specific amount of Li_2CO_3 and sintered in a tube furnace at a heating rate of 5 °C min^{-1} to a target temperature. To optimize the regeneration conditions, different sintering temperatures (700 °C, 750 °C, 800 °C, and 850 °C) and sintering times (1, 2, 4, and 6 hours), as well as varying Li_2CO_3 dosages (5%, 10%, and 20% excess relative to the total amount of Ni + Co + Mn), were applied, and the regenerated NCM70 (RNCM70) materials were systematically characterized.

Material characterization

X-ray diffraction (XRD) patterns of the samples were collected using a Malvern Panalytical Empyrean equipped with Cu Kα radiation. Rietveld refinement of the XRD patterns was performed using General Structure Analysis System-II (GSAS-II) software. The morphology and microstructure of the samples were examined using scanning electron microscopy (SEM, Hitachi SU8230, Japan) under an acceleration voltage of 10 kV and a beam current of 30 μA, and high-resolution transmission electron microscopy (HRTEM, Thermo Scientific Talos 200×) was employed to study the microstructure in detail. The chemical composition of the materials was analyzed using X-ray photoelectron spectroscopy (XPS, ESCALAB 250 XI). Additionally, the elemental content of the materials before and after regeneration was determined using inductively coupled plasma optical emission spectrometry (ICP-OES, PerkinElmer Avio 200). Dynamic light scattering (DLS) was conducted using a Zetasizer Nano ZS90 (Malvern Ltd, UK). The thermal stability of the materials was evaluated through thermogravimetric analysis (TGA, METTLER TOLEDO TGA2).

Electrochemical performance characterization

The electrochemical performance of all the samples was evaluated by fabricating coin half-cells. The cathode slurry was prepared by mixing the active material, acetylene black, and PVDF binder in NMP solvent at a weight ratio of 8 : 1 : 1 The slurry was then coated onto aluminum foil and dried in a vacuum oven at 120 °C for 12 hours. The dried cathodes were cut into circular discs with a diameter of 12 mm and coupled with Li metal and LP40 electrolyte (1 M $LiPF_6$ in ethylene carbonate/diethyl carbonate) to fabricate the cells. The voltage profiles and cycling performance were tested using a Neware battery test system, and electrochemical impedance spectra (EIS) were recorded on a CHI660c electrochemical workstation.

Results and discussion

Homogenization of DNCM70

Fig. S1† presents the optical image of a waste NCM70 battery retired from an electric bicycle. Following complete dischar-

ging, the battery was carefully disassembled following the flowchart illustrated in Fig. 1a, with procedural details provided in the Experimental section. The collected DNCM70 powder was initially characterized by SEM to investigate its morphological evolution after service. As shown in Fig. S2,† the original spherical polycrystals of NCM70 are significantly degraded after extended cycling. Pronounced intergranular cracks along grain boundaries, coupled with varying degrees of particle fragmentation, are clearly evident (Fig. 1b). This microscale mechanical degradation, observed in high-Ni NCM materials, is primarily attributed to anisotropic lattice expansion and contraction during Li^+ intercalation and deintercalation.[15,16] Such processes induce boundary strain among primary particles, resulting in intergranular cracks and the breakdown of secondary particles.[10,11] It should be noted that this mechanical degradation presents significant challenges for the direct regeneration of these materials.

To address this, ball milling pretreatment was employed to homogenize the particle size of DNCM70. The SEM images of the resulting HCNM70 are shown in Fig. S3 and S4† and Fig. 1c–f. At lower speeds, such as 450 and 540 rpm, the secondary particles cannot be fully destroyed (Fig. S3† and Fig. 1c and d). As the milling speed increases, secondary particles are almost entirely fragmented into primary particles (Fig. S4† and Fig. 1e and f). The particle size distribution of the homogenized materials was further analyzed using DLS (Fig. 1g–k). Samples milled at a low speed of 450 rpm exhibit a broad size distribution ranging from 295.3 nm to 955.4 nm, which becomes narrow when the milling speed is increased. At a high speed of 630 or 750 rpm, the size distribution converges to a range of 220.2 nm to 615.1 nm, closely matching the size of primary particles, indicating that further fragmentation of primary particles is not easy. This homogenization effect is attributed to the weakened adhesion between primary particles caused by cycling, as reported previously.[17] Consequently, mild ball milling facilitates fragmentation along grain boundaries, enabling effective size homogenization of degraded polycrystalline secondary particles.

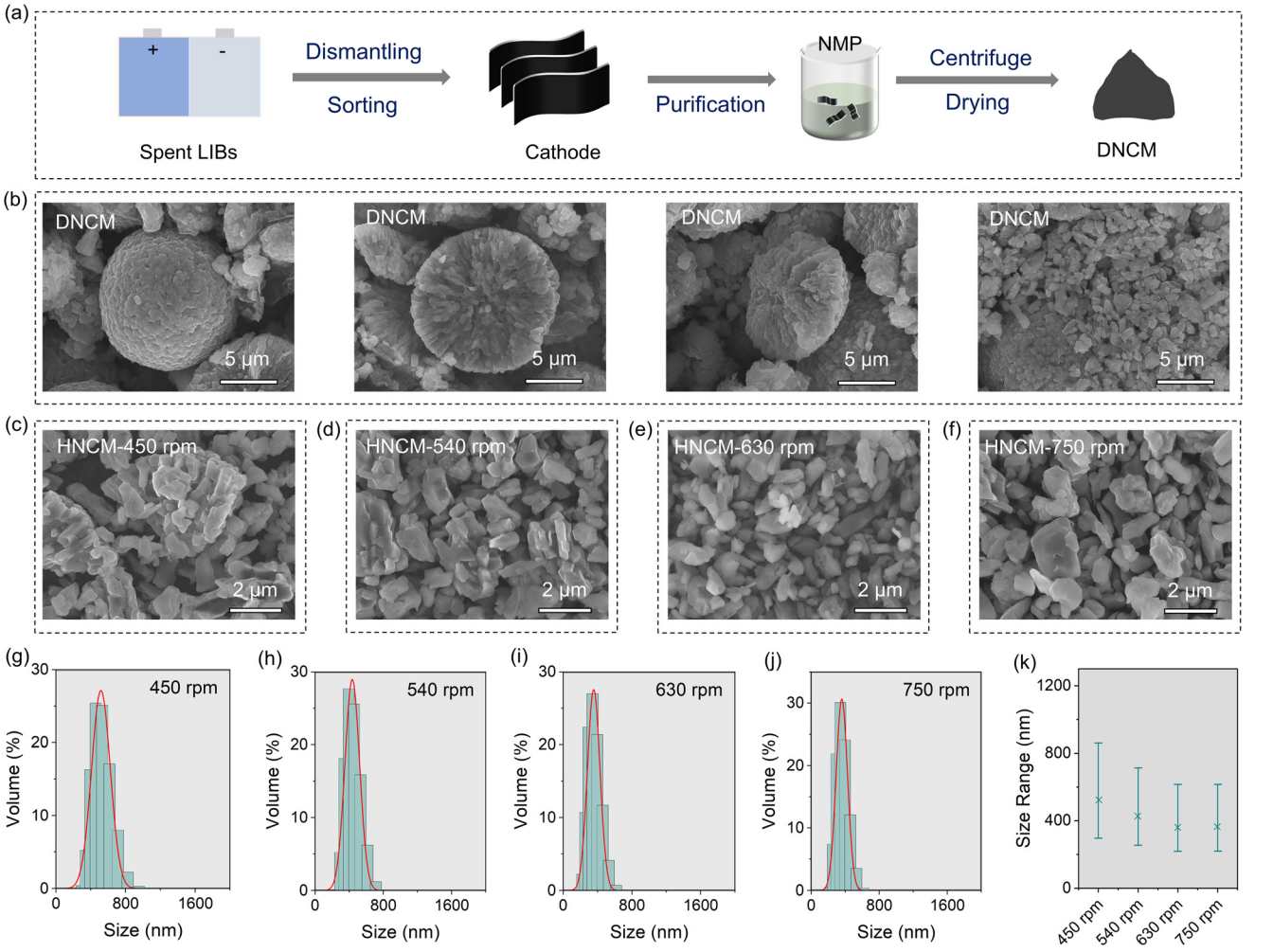

Fig. 1 (a) Schematic illustration of the disassembly process of the waste NCM70 battery; (b) SEM images of DNCM70; (c–f) SEM images of HDNCM70 milled at 450, 540, 630, and 750 rpm; (g–j) DLS results of HDNCM70 milled at different speeds, with the corresponding size distribution summarized in (k).

To confirm whether the core structure is maintained after milling, XRD analysis was performed on the HDNCM70 materials. As depicted in Fig. S5,† the XRD patterns reveal that all the materials after ball milling at various speeds retain a well-defined layered α-$NaFeO_2$ structure with the $R\bar{3}m$ space group.[18] No additional peaks related to impurity phases are observed, indicating that no significant phase transitions occurred during the milling process. However, the sample milled at 750 rpm exhibits weak peak intensity, suggesting reduced crystallinity.[19] Additionally, a leftward shift of the (003) peak is observed for this sample, indicating a loss of lattice-Li during the milling process.[20] This is further confirmed by the ICP results. The Li content of the materials after ball milling at rates of 450, 540 and 630 rpm is similar to that of DNCM70. However, a slight decrease in Li content is observed in the sample milled at 750 rpm, potentially caused by the leaching of Li^+ by the ethanol medium at a high milling speed. Therefore, a milling speed of 630 rpm, which provides effective grinding and uniform size distribution without compromising the crystal structure, is identified as the optimal condition for particle size homogenization in this study.

Regeneration of HDNCM70

The HDNCM70 obtained after ball milling was regenerated *via* a simple solid-state sintering process, with systematic optimization of temperature, duration, and Li_2CO_3 dosages. Fig. 2a and Fig. S6 and S7† show the XRD results and SEM image of the resulting RNCM70 sintered at different temperatures. All sintered samples exhibit smooth, clean surfaces with no visible cracks after sintering (Fig. S6†). However, at a sintering temperature of 850 °C, some aggregation of primary particles is observed, likely due to the Ostwald ripening effect.[21]

The XRD patterns in Fig. 2a indicate that all the RNCM70 samples display diffraction peaks that correspond well with the layered structure, with no detectable impurity phases. Additionally, the (003) peak gradually shifts to higher diffraction angles as the sintering temperature increases from 700 °C to 750 °C and stabilizes when the temperature is further increased. This indicates that full relithiation occurs around 750 °C, likely because this temperature is close to the decomposition temperature of Li_2CO_3 (723 °C), facilitating the replenishment of Li^+ into the lattice.[22,23]

The intensity ratio of the (003) and (104) peaks in the XRD patterns was further analyzed to evaluate the structural ordering

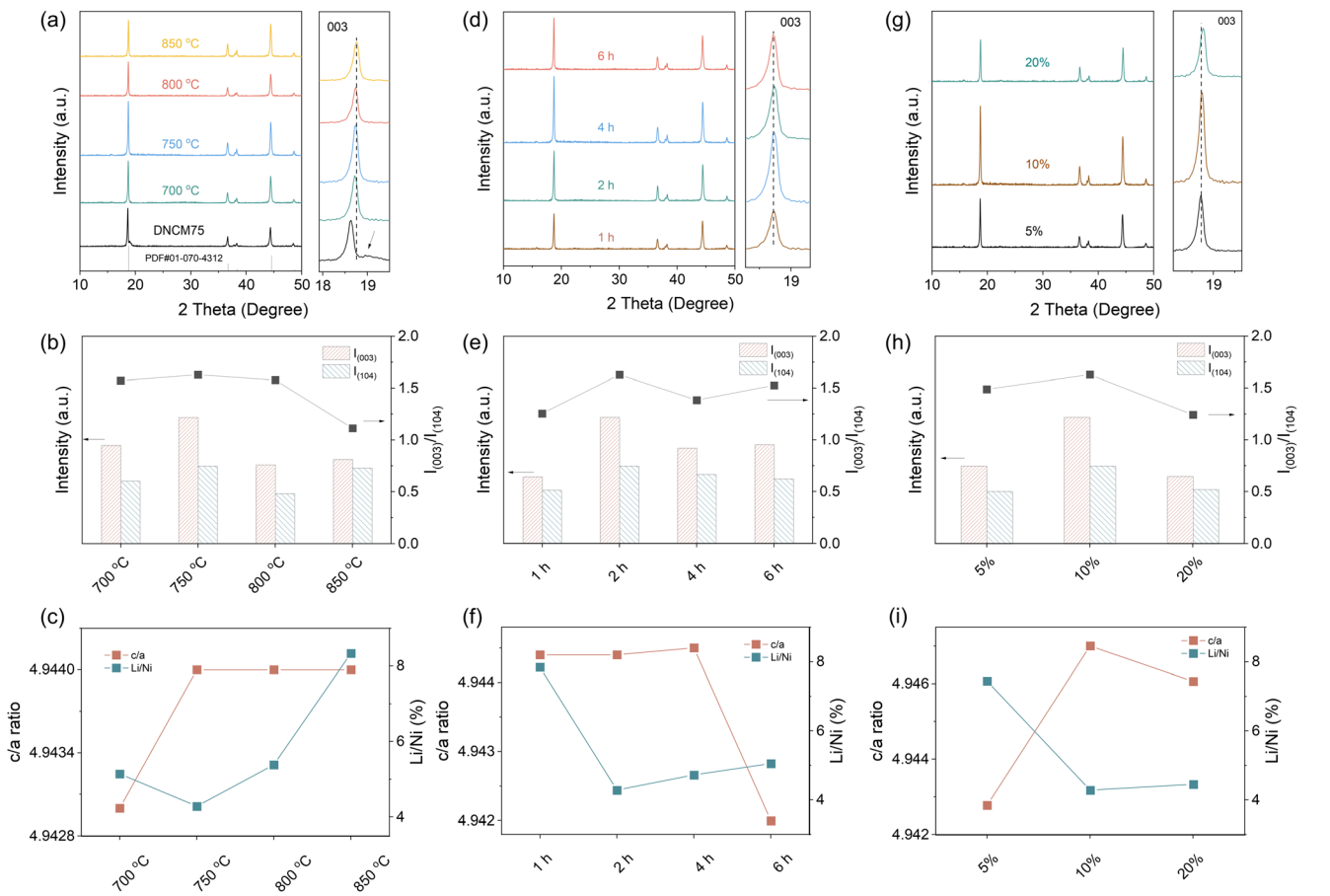

Fig. 2 (a) XRD patterns, (b) $I_{(003)}/I_{(104)}$ ratios and (c) *c*/*a* ratios and Li/Ni mixing of RNCM70 sintered at 700 °C, 750 °C, 800 °C, and 850 °C; (d) XRD patterns, (e) $I_{(003)}/I_{(104)}$ ratios and (f) *c*/*a* ratios and Li/Ni mixing of RNCM70 sintered at 750 °C for 1, 2, 4, and 6 hours; (g) XRD patterns, (h) $I_{(003)}/I_{(104)}$ ratios and (i) *c*/*a* ratios and Li/Ni mixing of RNCM70 sintered at 750 °C with 5%, 10%, and 20% excess Li_2CO_3.

of the RNCM70 materials. As shown in Fig. 2b, the samples sintered at 700 °C–800 °C exhibit a similar $I_{(003)}/I_{(104)}$ ratio of around 1.57, which decreases to 1.11 for the sample sintered at 850 °C, indicating significant cation mixing.[24,25] This is attributed to the accelerated Li^+ evaporation from the nanosized particles during high-temperature sintering, promoting Ni migration from the 3b to the 3a site in the lattice.[24,26]

To gain further insight into the structural characteristics, XRD Rietveld refinement was then performed to determine the unit cell parameters *c* and *a*, their ratios, and Li/Ni mixing (Fig. 2c). Compared to the samples sintered at other temperatures, the RNCM70 sintered at 750 °C displays the highest *c*/*a* ratio of 4.94 and the lowest Li/Ni mixing of 4.28, suggesting a well-ordered layered structure.[27] Therefore, further optimization of sintering duration and Li_2CO_3 dosages was carried out based on this temperature.

Fig. S8 and S9† and Fig. 2d–f display the SEM images and XRD patterns, along with the refinement results, of the RNCM70 sintered at 750 °C for different durations. It is evident that the sintering duration does not significantly affect the morphology of RNCM70 (Fig. S8†), but it affects the structure of the resulting materials. The sample sintered for 2 hours exhibits a higher intensity ratio of the (003) and (104) peaks and a lower Li/Ni cation mixing. Extending the sintering duration leads to increased cation mixing due to the rapid evaporation of Li^+ ions from the lattice.[28]

The effect of Li_2CO_3 content on the regeneration of DNCM70 was then investigated. The SEM images in Fig. S10† show that the samples sintered with 5% and 10% excess Li_2CO_3 exhibit similar individual granular morphology. However, when the Li_2CO_3 content exceeds 20%, particle aggregation becomes evident. This is due to the excess Li_2CO_3 forming a molten state during heating, with subsequent solidification during cooling, which promotes particle agglomeration.[29]

The XRD patterns and the corresponding Rietveld refinement results shown in Fig. 2g–i and Fig. S11† indicate that when Li_2CO_3 is added in excess of 5%, the RNCM70 exhibits high Li/Ni cation mixing (4.28%). This is primarily due to the slower replenishment of Li^+ into the lattice compared to its evaporation, leading to vacancies in the lattice and promoting cation mixing.[30] When the Li_2CO_3 content is increased to 10% excess, the resulting RNCM70 maintains a well-defined layered structure, as indicated by the high intensity ratio of the (003) and (104) diffraction peaks and a high *c*/*a* ratio. Further increasing the content of Li_2CO_3 leads to a decrease in the intensity of the diffraction peaks and a slight increase in cation mixing.

The Li contents in the RNCM70 materials regenerated under different conditions were measured *via* ICP, and the results are summarized in Fig. 3a with commercial NCM70 (CNCM70) for comparison. Notably, all the samples were care-

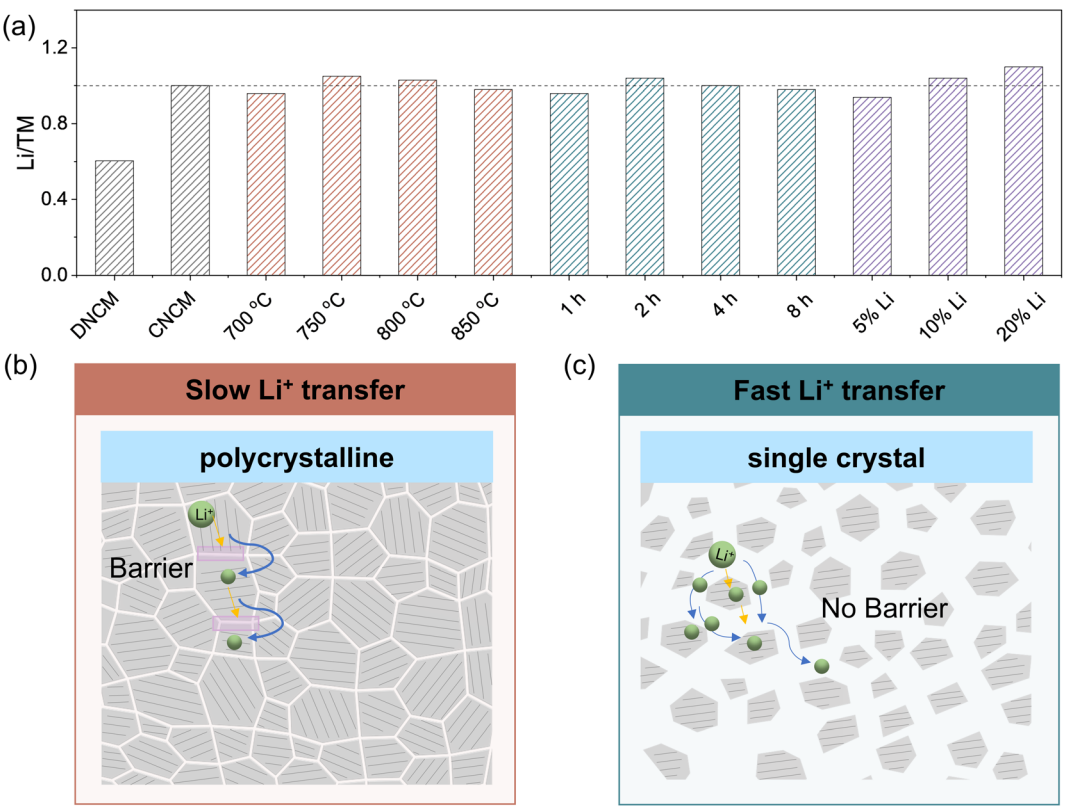

Fig. 3 (a) The Li contents in RNCM70 under different conditions; (b and c) schematic illustration of the Li^+ diffusion pathway in polycrystalline and single-crystalline NCM particles.

fully washed with water to remove excess surface Li. Compared to DNCM70, the Li content in all RNCM materials is significantly increased. However, the RNCM70 samples sintered at a low temperature of 700 °C or with a short duration of 1 hour, as well as those regenerated with a low amount of Li_2CO_3, exhibit lower Li content than the stoichiometric ratio, indicating insufficient relithiation under these conditions. In contrast, sintering at 750 °C for 2 hours fully restores the Li inventory in NCM, with a temperature lower and duration shorter than in previous reports on NCM cathode regeneration.[31–33] This suggests rapid Li^+ diffusion kinetics within the HDNCM70 lattice. However, higher sintering temperatures or longer sintering durations resulted in reduced Li content in the lattice, likely due to the rapid evaporation of Li from the particles.

To verify the size effect on efficient relithiation under these milder conditions, DNCM70 without ball milling pretreatment was sintered under the same conditions. As depicted in Fig. S12,† the XRD results demonstrate that the (003) peak of the RNCM70 without ball milling shows a lower diffraction angle compared to that of the RNCM70 with ball milling pretreatment, indicating incomplete lithiation.[21,34] The ICP results further reveal that the Li content is only 0.82 for the RNCM70 sample regenerated without ball milling. The low $I_{(003)}/I_{(104)}$ ratio of 0.94 further demonstrates severe cation mixing in this sample.[35] Additionally, the repaired NCM70, without ball milling, demonstrates a lower capacity compared to the ball-milled cathode. Therefore, under the same conditions, DNCM70 cannot be regenerated without homogenization treatment. This is primarily because the grain boundaries of the polycrystalline particles act as barriers to Li^+ transfer, resulting in slow Li^+ diffusion during the relithiation process (Fig. 3b). In contrast, the nanostructured primary particles after homogenization expose more surface for Li^+ diffusion, shortening the Li^+ diffusion pathway and enabling efficient regeneration under mild conditions (Fig. 3c).

Material characterization of RNCM70

The chemical composition and microstructural recovery of the NCM material upon regeneration at 750 °C for 2 hours with 10% excess Li_2CO_3 were then investigated *via* XPS and HRTEM. Fig. 4a compares the O 1s XPS spectra of NCM70 before and after regeneration. Prior to regeneration, the O 1s spectrum of DNCM70 shows three deconvoluted peaks at 529.4 eV, 530.1 eV, and 531.5 eV, corresponding to the oxygen in the layered structure, the rock-salt phase (NiO), and surface impurities containing HCO_3^-/CO_3^{2-}, respectively (Fig. 4b).[36] After regeneration, the peak associated with the rock-salt phase disappears, indicating phase recovery. But the peak attributed to CO_3^{2-}/OH^- remains pronounced, primarily due

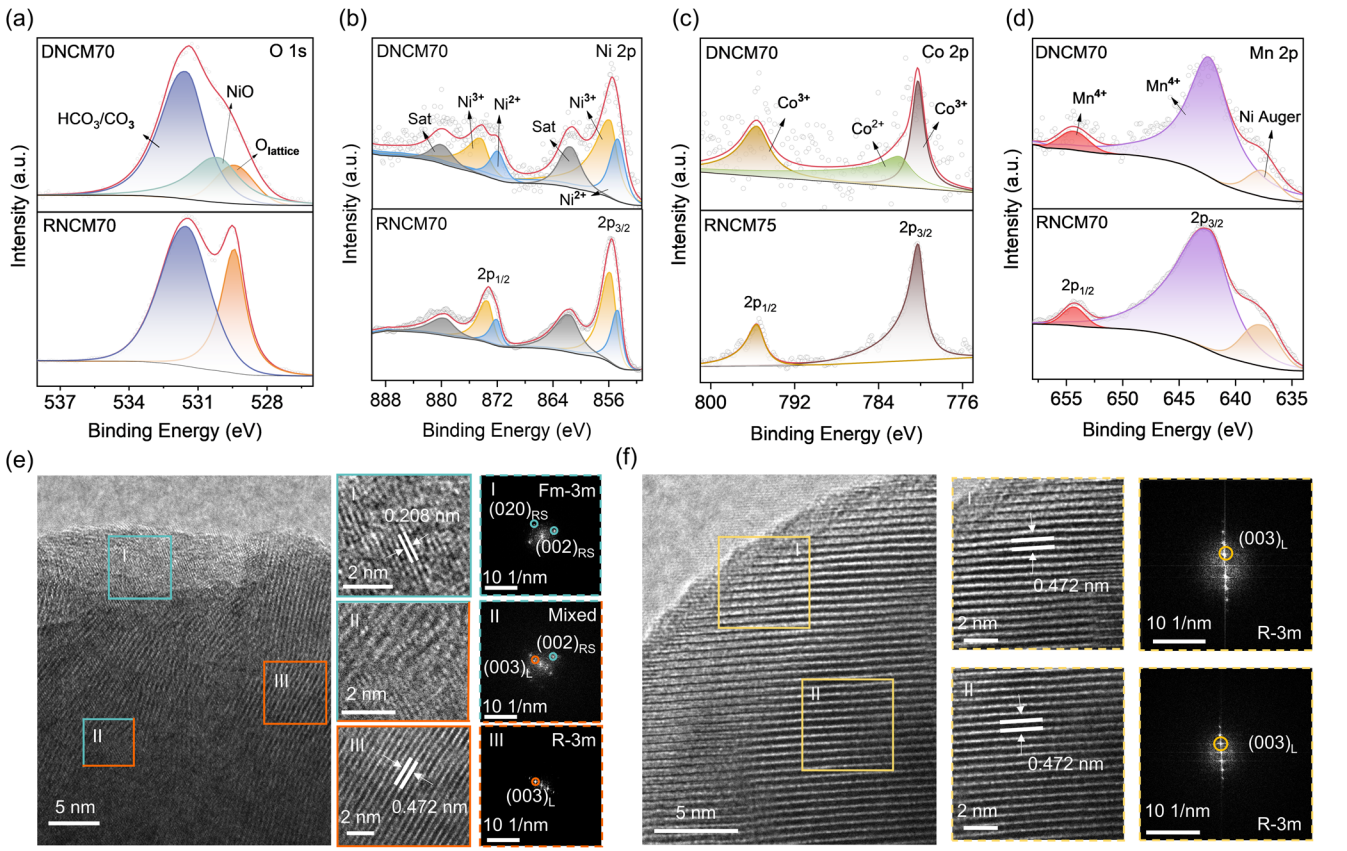

Fig. 4 (a–d) XPS spectra of NCM70 before and after regeneration; (e and f) HRTEM images and the corresponding FFT patterns of DNCM70 and RNCM70.

to the addition of excess Li_2CO_3 during the regeneration process.

Fig. 4b–d present the XPS spectra of transition metals. Obviously, the RNCM70 spectra exhibit higher peak intensities, indicating the removal of surface impurities and the exposure of a cleaner surface post-regeneration. In the Ni 2p spectra, both DNCM70 and RNCM70 feature two main peaks at 873.1 eV and 855.5 eV, attributed to Ni $2p_{1/2}$ and Ni $2p_{3/2}$, along with two satellite peaks at 879.8 eV and 861.2 eV.[37] Fitting these main peaks reveals Ni in the +2 and +3 oxidation states. Notably, the Ni^{3+} content increases from 62% to 84% after regeneration, further signifying a phase transformation from the rock-salt phase to the layered structure.

In the Co 2p XPS spectra (Fig. 4c), two main peaks corresponding to Co $2p_{3/2}$ and Co $2p_{1/2}$ are observed at 780.2 eV and 795.6 eV for both samples. It should be noted that DNCM70 exhibits relatively wide peaks, which can be further deconvoluted into two peaks at 781.5 eV and 780.2 eV, corresponding to Co^{2+} and Co^{3+}, respectively, indicating the presence of a spinel phase such as Co_3O_4 in the degraded cathode material.[38] Following regeneration, the Co^{2+}-related peak disappears and Co exists primarily in the +3 oxidation state in RNCM70, confirming phase restoration in this process. In the Mn 2p spectra, two peaks corresponding to Mn $2p_{1/2}$ and Mn $2p_{3/2}$ are observed at 654.3 eV and 642.3 eV, respectively, which remain unchanged before and after regeneration, indicating that Mn retains a stable +4 oxidation state throughout the degradation and regeneration processes.

We then conducted TG characterization to evaluate the thermal stability of the regenerated materials (Fig. S13†). Below 200 °C, RNCM70 and DNCM70 exhibit a similar weight loss due to the evaporation of absorbed H_2O. In the temperature range of 200 °C and 650 °C, DNCM70 exhibits obvious weight loss due to the loss of O_2 resulting from the phase change from the layered structure to spinel and rock-salt phases. In contrast, RNCM70 does not show obvious weight loss during the heating process, indicating a stable structure after regeneration.

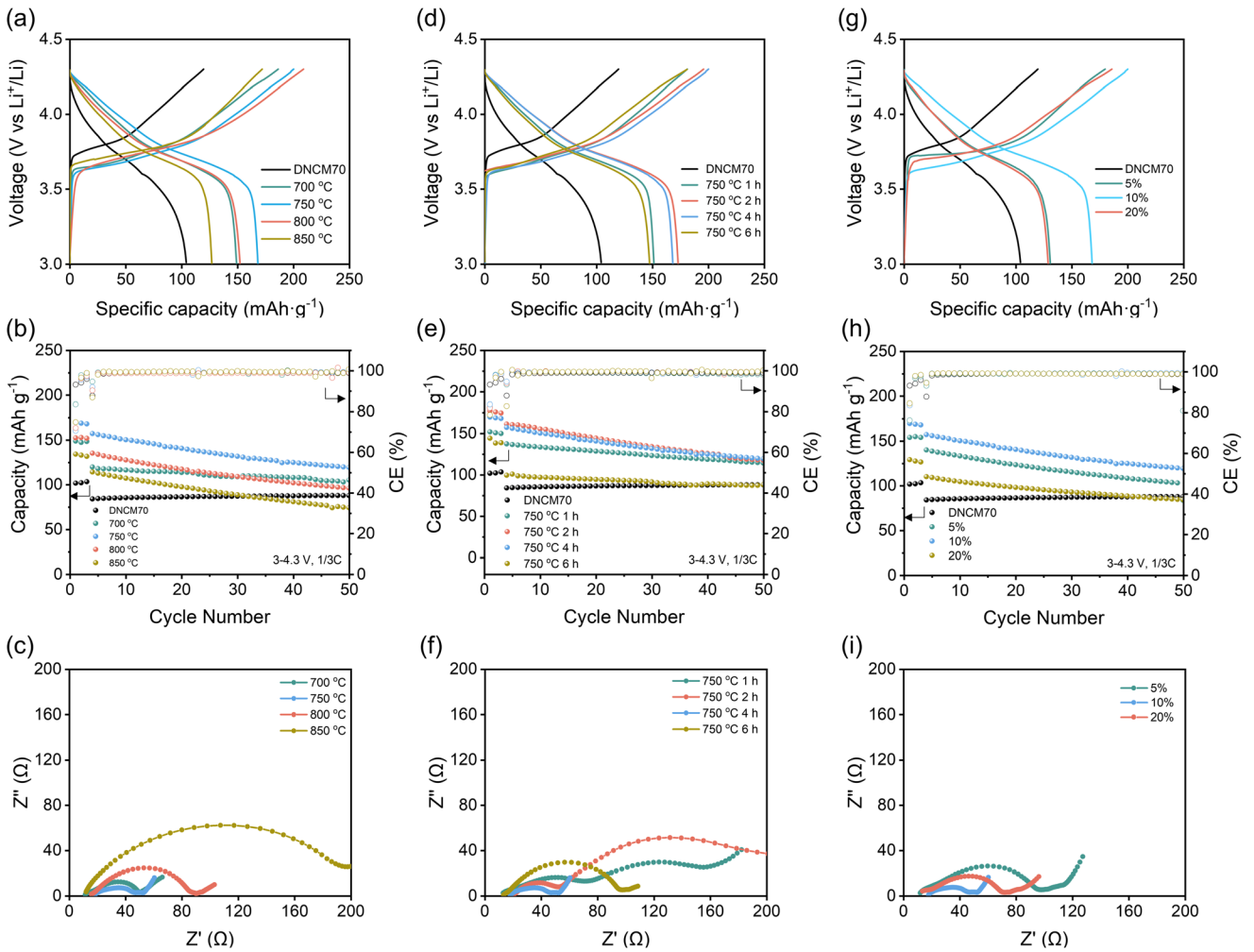

Fig. 5 (a–c) Voltage profiles, cycling performance and Nyquist plots of RNCM70 sintered at 700 °C, 750 °C, 800 °C, and 850 °C; (d–f) voltage profiles, cycling performance and Nyquist plots of RNCM70 sintered at 750 °C for 1, 2, 4, and 6 hours; (g–i) voltage profiles, cycling performance and Nyquist plots of RNCM70 sintered at 750 °C with 5%, 10%, and 20% excess Li_2CO_3.

The HRTEM images and the fast Fourier transform (FFT) diffraction patterns of DNCM70 and RNCM70 are displayed in Fig. 4e and f. The HRTEM image (Fig. 4e) of DNCM70 reveals lattice fringes with varied orientations, analyzed in three representative regions. Region III shows well-defined lattice fringes with a spacing of 0.472 nm, corresponding to the (003) plane of the layered structure. Region II displays disordered fringes, with FFT patterns indicating a mix of layered and rock-salt phases. In region I, the lattice fringe spacing is reduced to 0.208 nm, and diffraction patterns reveal only the (002) plane of the rock-salt phase, indicating a complete transformation of the layered structure to the rock-salt phase on the particle surface. In contrast, RNCM70 exhibits uniformly oriented lattice fringes with a consistent spacing of 0.472 nm, corresponding to the (003) plane of the layered structure (Fig. 4f). These findings collectively suggest that although prolonged cycling induces phase transitions in the layered structure and the formation of substantial impurities on the particle surface, these issues are effectively resolved through solid-state sintering regeneration.[39]

Electrochemical performance characterization of RNCM70

The electrochemical performance of RNCM70 materials regenerated under various conditions was systematically investigated, with the results displayed in Fig. 5. The charge–discharge test was conducted in the voltage range of 3.0 to 4.3 V at 0.1C (1C = 200 mA g^{-1}). Cycling performance was evaluated by activation at 0.1C for 3 cycles, followed by 50 cycles at 1/3C. Fig. 5a shows the voltage profiles of RNCM70 sintered at different temperatures. DNCM70 exhibits a low discharge capacity of 104.2 mA h g^{-1}, primarily due to compositional and structural defects in the lattice after cycling. After sintering with controlled amounts of Li_2CO_3, the specific capacity is significantly improved. Specifically, RNCM70 sintered at 700 °C, 750 °C, 800 °C, and 850 °C exhibits discharge capacities of 149.3 mA h g^{-1}, 168.4 mA h g^{-1}, 152.4 mA h g^{-1}, and 127.1 mA h g^{-1}, respectively. Among these, the sample sintered at 750 °C exhibits the highest capacity. This is attributed to the fact that a low temperature of 700 °C is insufficient to fully replenish Li vacancies in the lattice, as it is below the decomposition temperature of Li_2CO_3. Conversely, sintering at temperatures above 750 °C leads to Li^+ evaporation from the nanoparticles. After 50 cycles, the RNCM70 sintered at 750 °C still retains a capacity of 119.2 mA h g^{-1}, which is significantly higher than those of samples sintered at other temperatures (Fig. 5b).

Fig. 5c presents the Nyquist plots of RNCM70 materials, showing a semicircle in the high-frequency region and a sloping line in the low-frequency region, corresponding to charge-transfer resistance (R_{ct}) and Warburg resistance, respectively. The intersection of the semicircle with the x-axis represents the Ohmic resistance (R_s). Although all samples displayed similar R_s values, notable differences were observed in R_{ct}. The RNCM70 sintered at 750 °C exhibited the lowest R_{ct} of 33.72 Ω, compared to 37.19 Ω, 69.68 Ω, and 188.13 Ω of the samples sintered at 700 °C, 800 °C, and 850 °C, respectively, indicating superior electrochemical kinetics of this sample, which is mainly attributed to the well-restored structure and reduced cation mixing.

The voltage profiles for RNCM70 sintered at 750 °C for varying durations are shown in Fig. 5d. Among these, the sample sintered for 2 hours achieved the highest initial capacity of 173.1 mA h g^{-1}, with 117.4 mA h g^{-1} retained after 50 cycles (Fig. 5e). The corresponding EIS results in Fig. 5f reveal that this sample exhibits the smallest R_{ct} (32.16 Ω) compared with the others. This indicates that a short duration of 2 hours can enable the regenerated material to achieve high performance, suggesting rapid relithiation kinetics during the regeneration process.

Fig. 5g and h show the voltage profiles, cycling performance, and EIS results for RNCM70 regenerated with different amounts of Li_2CO_3. When 5% excess Li_2CO_3 was added, a capacity of only 130.9 mA h g^{-1} was achieved, likely due to a higher Li^+ evaporation rate than the relithiation rate, resulting in insufficient Li^+ in the final product. With 10% excess Li_2CO_3, the capacity increased to 168.4 mA h g^{-1}. However,

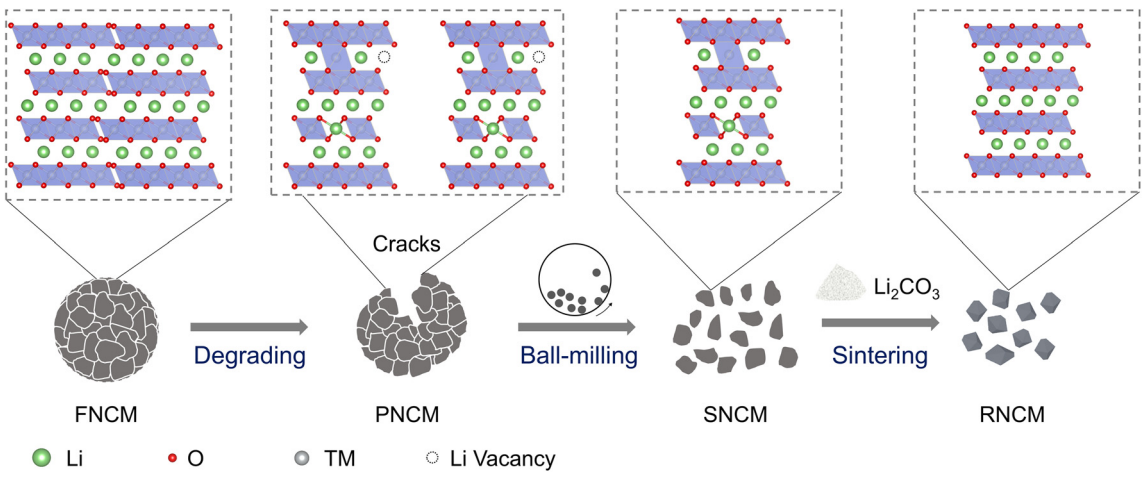

Fig. 6 Schematic illustration of the direct regeneration of mechanically degraded NCM70.

using 20% excess Li_2CO_3 reduced the capacity to 129.0 mA h g^{-1} due to residual Li in the regenerated material. After 50 cycles, RNCM70 regenerated with 10% excess Li_2CO_3 retained a capacity of 117.4 mA h g^{-1} and exhibited stable cycling performance. Additionally, it displayed the lowest R_{ct} among the samples (Fig. 5i). Overall, we employed ball-milling pretreatment to achieve particle homogenization of mechanically degraded Ni-rich cathode materials. Combined with solid-state regeneration, this approach significantly improved the structure, composition, and electrochemical performance of the materials (Fig. 6).

Conclusions

In summary, DNCM70 experienced severe intergranular cracking and particle fragmentation after prolonged use in electric bicycles. These microscale mechanical degradations pose significant challenges to the direct regeneration of such materials through simple relithiation and sintering. This study successfully achieved morphological reconstruction and size homogenization of DNCM70 *via* mild ball milling, leveraging the weakened interactions between primary particles in polycrystals resulting from long-term cycling. The resulting HDNCM70 nanoparticles provided abundant facets for Li^+ diffusion, significantly shortening the diffusion pathway compared to secondary polycrystal particles. This enabled efficient relithiation at a low temperature of 750 °C with a short processing time of 2 hours, restoring the compositional and structural defects in DNCM70 and improving its capacity from 104.2 to 173.1 mA h g^{-1}. This work offers valuable insights into repairing cathodes with mechanical degradation and advances direct regeneration technology.

Author contributions

P. X. designed the experiment and supervised the project. X. L. and P. Y. conducted the experiments, data processing, and characterization. B. J. provided assistance in obtaining and analyzing HRTEM data and drafting the manuscript. J. C., G. W., Q. Z. and Q. Z. assisted in the revision of the manuscript. All authors discussed the results and commented on the manuscript.

Data availability

The data supporting this article have been included as part of the ESI.†

Conflicts of interest

No potential conflict of interest was reported by the authors.

Acknowledgements

P. Xu acknowledges funding from the National Natural Science Foundation of China (NSFC, 22208365), the Natural Science Foundation of Jiangsu Province (BK20220298), Gusu Innovation and Entrepreneur Leading Talents (ZXL2022463), and the Youth Promotion Association of Chinese Academy of Sciences (2023000079). The authors are also grateful for the technical support for Nano-X from the Suzhou Institute of Nano-Tech and Nano-Bionics, Chinese Academy of Sciences.

References

1 X. Lan, X. Xiong, J. Cui and R. Hu, *J. Energy Chem.*, 2023, **83**, 433–444.
2 J. Lin, X. Zhang, E. Fan, R. Chen, F. Wu and L. Li, *Energy Environ. Sci.*, 2023, **16**, 745–791.
3 B. Dunn, H. Kamath and J. M. Tarascon, *Science*, 2011, **334**, 928–935.
4 A. Soto, A. Berrueta, M. Mateos, P. Sanchis and A. Ursúa, *J. Energy Storage*, 2022, **55**, 105343.
5 A. Al-Amiery, W. N. R. Wan Isahak and W. K. Al-Azzawi, *Ain Shams Eng. J.*, 2024, **15**, 102672.
6 O. Dolotko, N. Gehrke, M. Knapp and H. Ehrenberg, *J. Alloys Compd.*, 2024, **976**, 172884.
7 P. Li, Q. Liu, M. Møller, D. Wang, L. R. Jensen and X. Xia, *Mater. Lett.*, 2024, **357**, 135724.
8 J. Zhou, X. Zhou, W. Yu, Z. Shang and S. Xu, *Electrochem. Energy Rev.*, 2024, **7**, 13.
9 N. Zhang, Z. Xu, W. Deng and X. Wang, *Electrochem. Energy Rev.*, 2022, **5**, 33.
10 J. M. Lim, T. Hwang, D. Kim, M. S. Park, K. Cho and M. Cho, *Sci. Rep.*, 2017, **7**, 39669.
11 S. Lee, L. Su, A. Mesnier, Z. Cui and A. Manthiram, *Joule*, 2023, **7**, 2430–2444.
12 H. Zhou, X. Zhao, C. Yin and J. Li, *Electrochim. Acta*, 2018, **291**, 142–150.
13 H. Dong, H. Wang, J. Qi, J. Wang, W. Ji, J. Pan, X. Li, Y. Yin and S. Yang, *ACS Sustainable Chem. Eng.*, 2022, **10**, 11587–11596.
14 H. Gao, Q. Yan, D. Tran, X. Yu, H. Liu, M. Li, W. Li, J. Wu, W. Tang, V. Gupta, J. Luo and Z. Chen, *ACS Energy Lett.*, 2023, **8**, 4136–4144.
15 H. H. Ryu, K. J. Park, C. S. Yoon and Y. K. Sun, *Chem. Mater.*, 2018, **30**, 1155–1163.
16 W. Li, H. Y. Asl, Q. Xie and A. Manthiram, *J. Am. Chem. Soc.*, 2019, **141**, 5097–5101.
17 K. Min and E. Cho, *Phys. Chem. Chem. Phys.*, 2018, **20**, 27115–27124.
18 D. Tang, D. Liu, Y. Liu, Z. Yang and L. Chen, *Prog. Nat. Sci.: Mater. Int.*, 2014, **24**, 388–396.
19 D. Chukhchin, A. Malkov, I. Tyshkunova, L. Mayer and E. Novozhilov, *Crystallogr. Rep.*, 2016, **61**, 371–375.
20 S. Li, Y. Sun, A. Gao, Q. Zhang, X. Lu and X. Lu, *Proc. Natl. Acad. Sci. U. S. A.*, 2022, **119**, e2120060119.

21 D. Mohanty, A. S. Sefat, J. Li, R. A. Meisner, A. J. Rondinone, E. A. Payzant, D. P. Abraham, D. L. Wood III and C. Daniel, *Phys. Chem. Chem. Phys.*, 2013, **15**, 19496–19509.
22 P. Pasierb, R. Gajerski, S. Komornicki and M. Rekas, *J. Therm. Anal. Calorim.*, 2001, **65**, 457–466.
23 B. Wu, Z. Lin, G. Zhang, D. Zhang, W. Zhang, G. Li, Y. Che, L. Chen, H. Wang, W. Li, M. Chen and G. Cao, *Energy Storage Mater.*, 2022, **53**, 212–221.
24 G. X. Wang, S. Zhong, D. H. Bradhurst, S. X. Dou and H. K. Liu, *J. Power Sources*, 1998, **76**, 141–146.
25 W. M. Seong, Y. Kim and A. Manthiram, *Chem. Mater.*, 2020, **32**, 9479–9489.
26 O. Tsutomu, U. Atsushi and N. Masatoshi, *J. Electrochem. Soc.*, 1993, **140**, 1862–1870.
27 B. H. Toby and R. B. Von Dreele, *J. Appl. Crystallogr.*, 2013, **46**, 544–549.
28 Y. Qu, Y. Mo, X. Jia, L. Zhang, B. Du, Y. Lu, D. Li and Y. Chen, *J. Alloys Compd.*, 2019, **788**, 810–818.
29 J. Fu, Y. Bai, C. Liu, H. Yu and Y. Mo, *Mater. Chem. Phys.*, 2009, **115**, 105–109.
30 J. Yang, G. Mao, T. Yao, L. Shen and Y. Yu, *Angew. Chem., Int. Ed.*, 2024, **63**, e202420413.
31 Z. Chi, J. Li, L. Wang, T. Li, Y. Wang, Y. Zhang, S. Tao, M. Zhang, Y. Xiao and Y. Chen, *Green Chem.*, 2021, **23**, 9099–9108.
32 Y. Han, Y. You, C. Hou, X. Xiao, Y. Xing and Y. Zhao, *J. Electrochem. Soc.*, 2021, **168**, 040525.
33 Z. Wu, X. Zhang, F. Cheng, Y. Tong, Y. Xue, J. An and Z. Fang, *J. Electroanal. Chem.*, 2025, **978**, 118901.
34 N. Yabuuchi, K. Yoshii, S. T. Myung, I. Nakai and S. Komaba, *J. Am. Chem. Soc.*, 2011, **133**, 4404–4419.
35 S. Wang, M. Yan, Y. Li, C. Vinado and J. Yang, *J. Power Sources*, 2018, **393**, 75–82.
36 L. Hartmann, C. H. Ching, T. Kipfer, M. Koch and H. A. Gasteiger, *J. Electrochem. Soc.*, 2022, **169**, 070516.
37 Z. Qin, Z. Wen, Y. Xu, Z. Zheng, M. Bai, N. Zhang, C. Jia, H. B. Wu and G. Chen, *Small*, 2022, **18**, e2106719.
38 D. Ko and S. Mhin, *Sensors*, 2023, **23**, 5380.
39 C. Xing, H. Da, P. Yang, J. Huang, M. Gan, J. Zhou, Y. Li, H. Zhang, B. Ge and L. Fei, *ACS Nano*, 2023, **17**, 3194–3203.